Supplemental Material: Extremely low-energy collective modes in a quasi-one-dimensional topological system

Z. X. Wei et al.

A. Experimental setup and sample preparation

The time-resolved transient reflectivity signals, $\Delta R(t)/R$, were measured based on a degenerate pump-probe scheme using a Ti:sapphire laser oscillator that produces $\sim$55 fs (FWHM) pulses at the sample position with a repetition rate of 80 MHz. The center wavelength can be tuned between 780 nm and 820 nm. The pump beam directs along the normal. The probe beam is incident at a $\sim$ 10 degree angle to the sample normal. Typically, the pump was kept p-polarized, while the polarization of the probe beam was kept s-polarized (perpendicular to the c-axis or parallel to the a-axis of the sample). The cross-polarization configuration is used to remove the initial coherent artifacts [1]. The ZrTe$_5$ single crystals with three different thicknesses of $\sim$0.1, 0.3 and 0.5 mm were studied in this work, and similar results were obtained. These crystals were prepared by the Te-assisted chemical vapor transport method [2] or molten Te flux growth [3]. All the measurements were taken in vacuum ($\sim 10^{-6}$ Torr).

B. Fit of relaxation processes characterized by τ_1 and τ_s

1. Necessity including the process characterized by τ_1

Necessity including the τ_1 process can be understood more easily by showing the ΔR data in short timescale. Fig. S1 evidently demonstrates that it is essential to include such τ_1 process in order to fit well the initial slow rising. Mathematically, failure of fitting the experimental ΔR data without τ_1 process arises from the initial rising time limited by convolution via the Gaussian function $G(t)$, i.e. $\sim$100 fs, which is far less than what we detected ($\sim$0.5 ps).
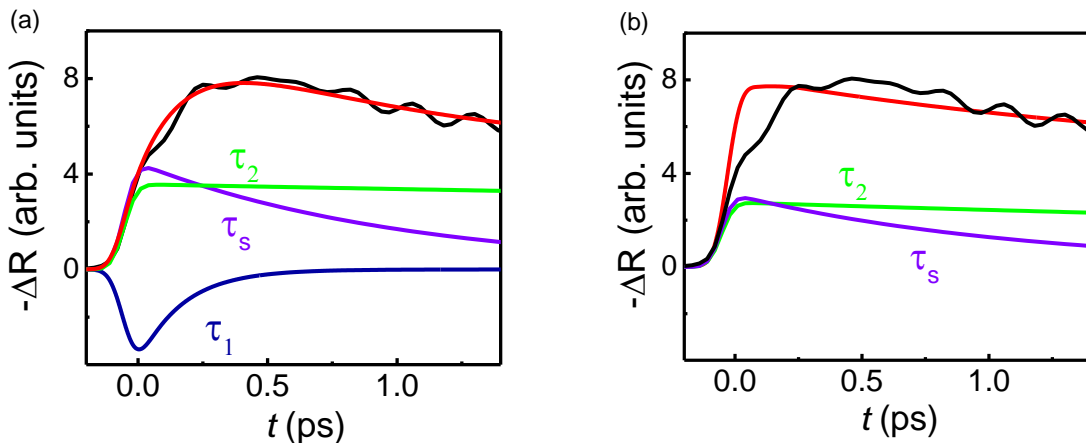

FIG. S1. The transient reflectivity $\Delta R(t)$ in short timescale measured at 5 K (black lines). We here employ the equation $\Delta R = [A_1 e^{-t/\tau_1} + A_2 e^{-t/\tau_2} + A_s e^{-t/\tau_s}] \otimes G(t)$ to fit the experimental data. $A_1 > 0$, $A_2 < 0$ and $A_s < 0$. The red lines are fitted curves (a) with and (b) without the τ_1 process that has amplitude with opposite sign.

2. Fit of relaxation time τ_1 and τ_s via the two-temperature mode (TTM)

Within TTM, the electron-phonon relaxation time τ_{e-ph} is given by[4, 5]:

$$\tau_{e-ph} = \frac{\gamma(T_e^2 - T_l^2)}{2H(T_e, T_l)}, \tag{1}$$

where γ is the electronic specific heat coefficient. Here,

$$H(T_e, T_l) = f(T_e) - f(T_l), \tag{2}$$

$$f(T) = 4g_{ep}\frac{T^5}{\theta_D^4}\int_0^{\theta_D/T} \frac{x^4}{e^x - 1}\,dx, \tag{3}$$

where T_e is the electron temperature after electron-electron (e-e) thermalization, which is initially higher than the lattice temperature T_l. g_{ep} is electron-phonon coupling coefficient. The T_e can be estimated by:

$$T_e = \sqrt{T_l^2 + \frac{2U_l}{\gamma}}, \tag{4}$$

where U_l is energy density of laser light. The fits to τ_1 and τ_s as a functions of temperature are given in the Figs. 2(a) and (e) of the main text, respectively. For τ_1, $\gamma = 0.65$ J·m^{-3}K^{-2} and $g_{ep} = 5.4 \times 10^{15}$ W·m^{-3}K^{-1}. For τ_s, $\gamma = 7.3$ J·m^{-3}K^{-2} and $g_{ep} = 1.9 \times 10^{15}$ W·m^{-3}K^{-1}. τ_1 and τ_s as functions of fluence are also given in the S2 (a) and (b), which can be well fitted using the TTM. Under the condition of $T_e - T_l \ll T_l$ (or low pump fluence regime), τ_{e-ph} can be approximated as: $\tau_{e-ph} \approx \frac{\pi k_B T_e}{3\hbar\lambda<\omega^2>}$ [4, 5]. Since T_e increases with the pump fluence increasing, τ_{e-ph} also becomes larger as the pump fluence increases.
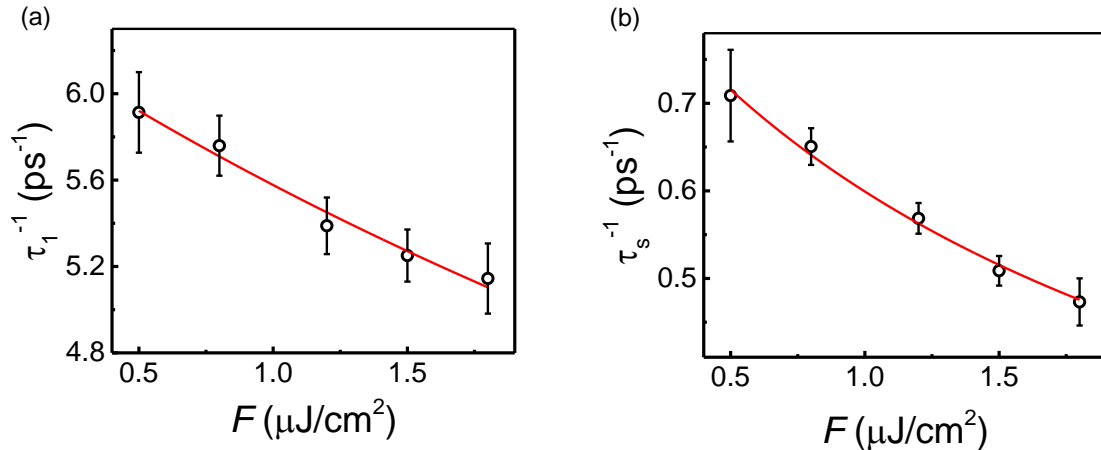

FIG. S2. (a) and (b) are τ_1 and τ_s as a function of fluence (F). The red solid lines are fit using the TTM.

C. Theoretical fit based on the phonon-assisted recombination process

The strongly temperature-dependent $\tau_2(T)$ can be quantitatively described by [6],

$$\frac{1}{\tau_2} = A\frac{\frac{\hbar\omega}{2k_B T}}{\sinh^2(\frac{\hbar\omega}{k_B T})} + \frac{1}{\tau_0}, \tag{5}$$

where ω corresponds to frequency of the phonon mode assisting e-h recombination. τ_0 represents a temperature independent recombination time which varies with sample quality. A is a parameter related to the density of states in the electronic energy bands and the matrix elements for interband e-h scattering. The fitted results agree quite well with the experimental τ_2 (see Fig. 2(c) in the main text), and strongly justify the presence of phonon-assisted e-h recombination.

D. Raman spectroscopy data and coherent oscillations via transient reflectivity measurements

We have carried out a detailed temperature-dependent Raman spectroscopy experiment on ZrTe$_5$. As shown in Fig. S3(a), the peaks indexed by 1, 4, 5, 6, and 7 stand for the A_g phonon modes, and another two indexed by 2 and 3 arise from the B_{2g} phonon modes [7, 8]. Based on Fig. 3 of the main text and Fig. S3, in addition to ω_1 and ω_2 modes, we clearly detected the Raman-active phonons indexed by 1, 5, and 6 via the oscillatory $\Delta R(t)/R$ signals. The close-neighboring modes indexed by 4 and 5, especially the former, have very low intensity and decay extremely fast, which lead to a relative broad feature in the Fourier transform spectra. The mode indexed by 7 is out of our detection limit. Since generation of the coherent optical phonons is associated with the Raman scattering process [9, 10], the amplitude of detected phonon is very sensitive to the pump or probe polarization of the laser beam relative to the crystal orientation (see Fig. S3(b) and (c)). Our experiment configuration only allows to initiate the A_g and B_{2g}
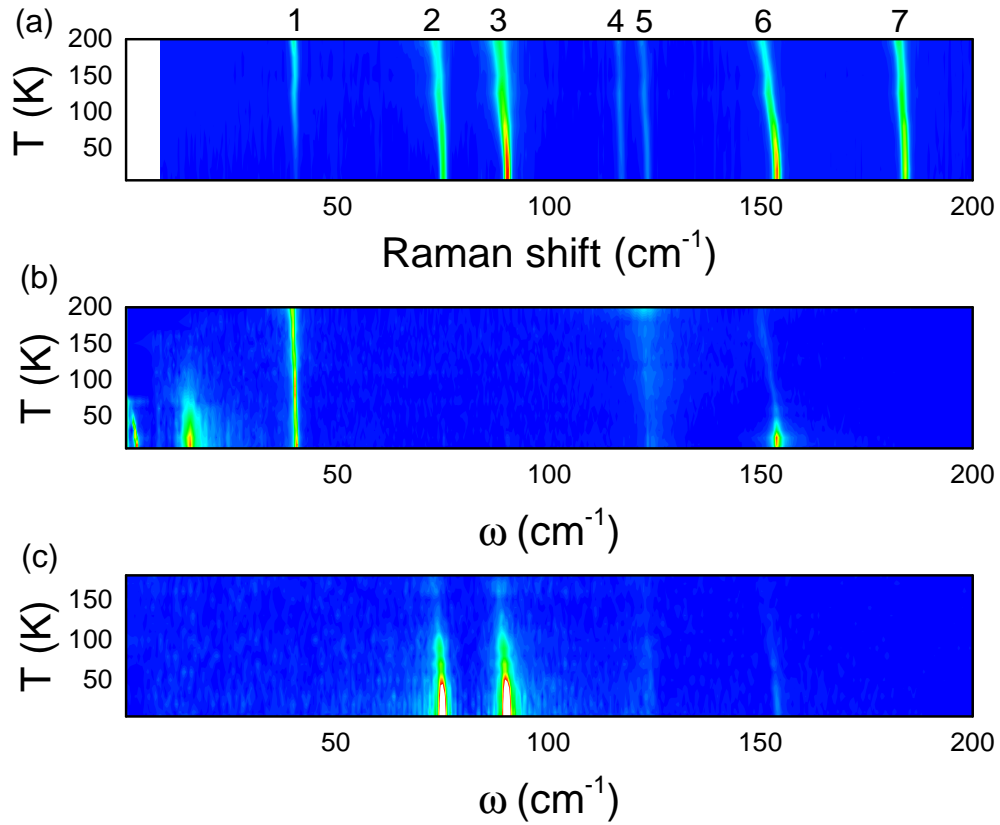
FIG. S3. (a) The temperature dependent Raman spectra of ZrTe$_5$. (b) and (c) The temperature-dependent Fourier transform spectra for the extracted oscillations. Signals in (c) were obtained via the anisotropic reflectivity measurements.

Raman modes in ZrTe$_5$ [7, 8]. In fact, based on the Raman tensor of B_{2g} mode, its dependence on the polarization has a sin2θ-like behavior and can be selectively extracted via the anisotropic reflectivity measurements [10], as seen in Fig. S3(c). The A_g modes are isotropic in contrast to the B_{2g} phonon modes. Some typical temperature-dependent transient reflectivity data at different wavelengths in the long-time domain are shown in Fig. S4, where various oscillation signals can be seen.
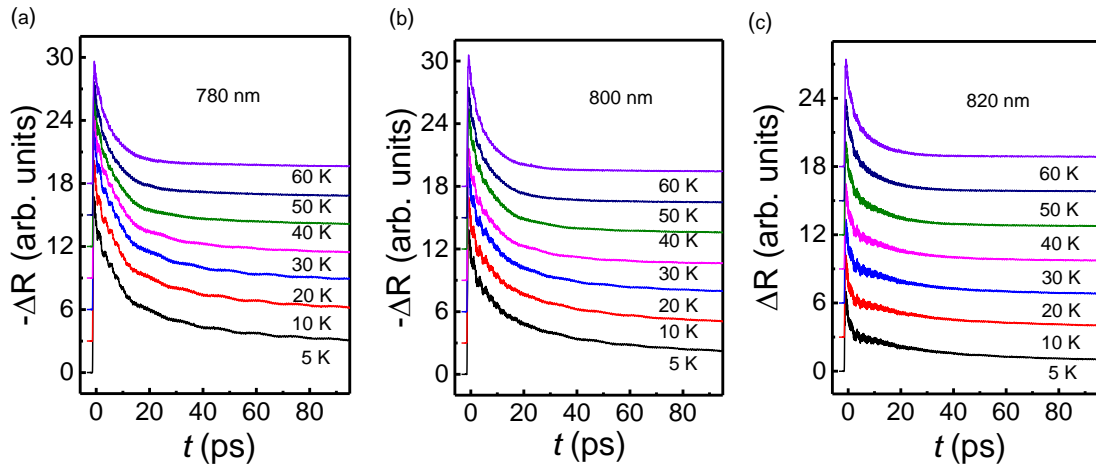

FIG. S4. The typical temperature-dependent transient reflectivity data measurements for different wavelengths in the long-time domain.

We note that the laser pulse chirping could affect the amplitudes of coherent optical phonons [11, 12]. However,

since the fs pulses arriving at the samples are nearly transform limited via our pulse compression system, this effect can be safely neglected. Moreover, even if there exists slight chirp effect, its influence on characterizing the sample quality can also be ignored due to the characteristic phonon frequencies remaining unchanged. Nonetheless, all these experimental data demonstrate that the ZrTe$_5$ samples we used have very high quality, which is a prerequisite for the further experiments. Note that we took the phonon mode with highest energy in the Raman data as the Debye frequency, which was used to extract the electron-phonon coupling constant λ [4].

E. Phonon renormalization as a function of temperature

Renormalization of the T-dependent optical phonons can be characterized by their frequencies (ω) and decay rates (Γ) in the temperature domain. Here, we mainly focus on discussing quantitatively $\omega(T)$ if not mentioned in the text. The typical ω results from the ultrafast experiments are shown in Fig. S5. Here, except the mode with frequency of $\sim$3.7 THz, in order to obtain ω, a sine damped equation $Ae^{-t/\tau}\sin(2\pi\omega t + \phi)$ was used to fit each oscillatory component extracted via different frequency filter in $\Delta R/R$ [13]. For the 3.7 THz mode (indexed by 5 in Fig. S3(a)), we directly extracted the T-dependent data by picking up the peak values in the Fourier transform spectra. The mode indexed by 8 with frequency larger than 200 cm^{-1} is not shown in Fig. S3 but is also listed here. All the detected Raman peaks (ω) as a function of temperature are given in Fig. S5. Clearly, results from both experiments agree very well, and demonstrate that there is no anomaly observed near T^*, which indicates no structural phase transition happening near T^*. Frequencies of the optical phonon modes in general present a softening behavior as the temperature increases. Such T-dependent behavior can be quantitatively explained by the anharmonic phonon model (solid line in Fig. S5)[14–16],

$$\omega(T) = \omega_0 + A_1[1 + 2n(\omega_0/2)] \tag{6}$$

where $\omega = 2\pi f, n(\omega) = [e^{\hbar\omega/k_B T} - 1]^{-1}$, ω_0 is the bare harmonic frequency. It can be seen that the fitted data are in excellent agreement with the experimental results.
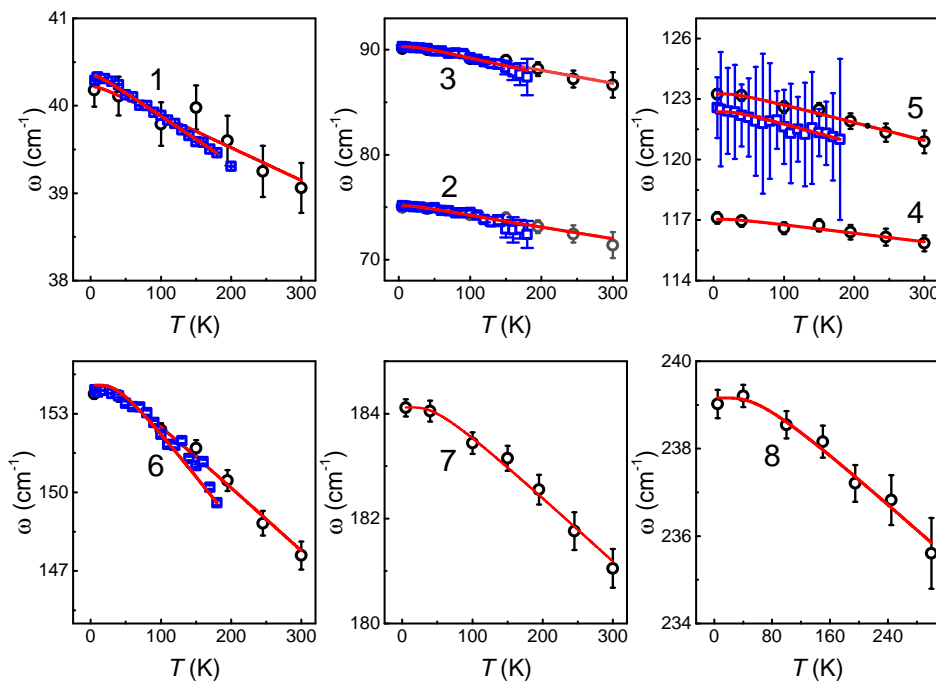

FIG. S5. Temperature dependence of the oscillation frequencies for optical phonon modes (blue open squares) extracted from the ultrafast experiments. For comparison, temperature dependence of Raman peaks (black open dots) in the frequency domain are also given. The red solid curves are fits to the data using Eq.6.The mode indexes follow those in Fig. S3(a).

Some detail temperature- and wavelength-dependent fitted parameters for two typical optical phonon modes are shown in Table I. It can be seen that their phases are nearly independent the temperature and wavelength. No π-phase change was observed in the experiment.

TABLE I. Some typical fitted parameters such as frequency, phase, and decay rate of the two main coherent optical phonon modes $\sim$1.2 THz and $\sim$4.6 THz as functions of wavelength and temperature.

wavelength (nm)	T (K)	Frequency (THz)	phase	decay rate (ps^{-1})	Frequency (THz)	phase	decay rate (ps^{-1})
780	5	1.20667±7.00114E-5	2.11933±0.00841	0.00877±3.31789E-4	4.63112±8.0385E-4	2.61005±0.02622	0.02727±0.00385
	10	1.20712±6.40336E-5	1.98387±0.00767	0.00913±3.03862E-4	4.62928±7.61999E-4	2.61048±0.02494	0.02398±0.00364
	20	1.20686±7.41145E-5	1.86184±0.00881	0.01012±3.53571E-4	4.62581±6.54729E-4	2.60061±0.0215	0.02024±0.00312
	30	1.20592±1.03262E-4	1.88142±0.00808	0.01245±3.36259E-4	4.62767±0.00101	2.62536±0.03286	0.0321±0.00488
	40	1.20555±6.99085E-5	1.79181±0.00808	0.01314±3.39915E-4	4.62767±0.00101	2.62536±0.03286	0.0321±0.00488
	50	1.20392±7.08476E-5	1.86106±0.00807	0.01466±3.47803E-4	4.61547±8.17102E-4	2.61801±0.02649	0.03293±0.00394
	60	1.20297±7.15908E-5	1.78258±0.00797	0.01687±3.56736E-4	4.60839±8.84727E-4	2.61967±0.02869	0.0323±0.00427
800	5	1.20835±5.05472E-5	1.81±0.0081	0.0067±1.60839E-4	4.62458±5.07587E-4	2.691±0.01606	0.06672±0.00244
	10	1.20772±4.10202E-5	1.84199±0.00649	0.0075±1.33648E-4	4.6223±3.62583E-4	2.99584±0.01041	0.09758±0.00189
	20	1.20827±5.68965E-5	1.90525±0.00862	0.00958±1.97633E-4	4.62697±7.78972E-4	2.74425±0.02307	0.08692±0.00395
	30	1.20845±9.11741E-5	2.17563±0.01271	0.01276±3.49924E-4	4.60439±7.545E-4	2.50554±0.02149	0.10053±0.00396
	40	1.20576±5.57588E-5	2.12886±0.00733	0.01489±2.2812E-4	4.61401±3.56615E-4	2.67556±0.01029	0.09588±0.00185
	50	1.20698±1.33617E-4	2.08186±0.0173	0.01542±5.54352E-4	4.61662±7.11324E-4	2.71663±0.01956	0.11276±0.00383
	60	1.20471±7.51236E-5	1.97628±0.00907	0.01804±3.33219E-4	4.63944±0.00443	2.74557±0.12128	0.11322±0.02376
	100	1.20245±2.48388E-4	1.946±0.02293	0.03211±0.00139	4.54677±0.01236	2.17987±0.09247	0.2917±0.07861
	200	1.18774±3.44249E-4	1.794±0.02868	0.04088±0.00199	4.46503±0.002375	2.63163±0.21952	1.05017±0.2636
820	5	1.21008±9.32163E-5	1.89947±0.01159	0.00318±4.33295E-4	4.62218±3.53213E-4	2.60055±0.01125	0.064833±0.00169
	10	1.21032±1.0428E-4	1.7643±0.01269	0.00681±4.89699E-4	4.61691±1.45505E-4	2.54113±0.00462	0.06604±6.96964E-4
	20	1.20859±6.76924E-5	2.00708±0.00818	0.00794±3.19627E-4	4.61433±1.8211E-4	2.53018±0.00572	0.06889±8.80744E-4
	30	1.20881±1.34098E-4	1.87505±0.01594	0.01±6.39376E-4	4.6169±2.53156E-4	2.59892±0.00761	0.08234±0.00127
	40	1.20677±7.68158E-5	2.20929±0.00899	0.01189±3.70235E-4	4.61475±3.63396E-4	2.6447±0.01071	0.08884±0.00185
	50	1.20585±8.73628E-5	2.07755±0.01017	0.01243±4.22808E-4	4.60542±0.00102	2.65125±0.02532	0.15286±0.00583
	60	1.20534±1.31413E-4	2.07668±0.01495	0.01467±6.45146E-4	4.59752±0.00119	2.703784±0.02768	0.17911±0.00696

F. More discussions about the coherent acoustic phonon

In fact, if the low frequency mode characterized by ω_1 or ω_2 is due to the coherent acoustic phonon, we can quantitatively estimate the frequency value of the corresponding oscillation for a given probe wavelength using the formula: $T = 1/f = \lambda_p(2nV_scos\theta)^{-1}$ (Refs. [56-58] in the main text). Here, T and f are the oscillation period and frequency, respectively. n is the refractive index. V_s is the sound velocity. λ_p is the angle of incidence of the probe light inside the sample with respect to the normal of sample surface. Using parameters $n \sim 2$ [17], $V_s \sim 10^3$ m/s (Ref. [62] in the main text), and $\theta \sim 0$ and $\lambda_p \sim 800$ nm, we can estimate the oscillation period is about 200 ps, whose corresponding frequency ($f = 1/T$) is clearly much lower than $\omega_1/2\pi$ and $\omega_2/2\pi$. Such result itself already can exclude the coherent acoustic phonon.

The change of period is related to the change of wavelength by the derived formula: $\Delta T = \Delta\lambda_p(2nV_scos\theta)^{-1}$. In our experiment, $\Delta\lambda_p$ can have a change of $\sim$40 nm, and then the corresponding ΔT is $\sim$10 ps, which is a huge variation in the oscillation signals. Accordingly, if ω_1 or ω_2 modes arise from the acoustic phonons, the frequency shift (Δf) could change by a factor of $\sim$1/2 for the ω_1 mode, and nearly by more than one order of magnitude for the ω_2 mode. In our experiment, we covered a time range of $\sim$0.5 ns with a time resolution of $\sim$10 fs, it is quite enough for detecting the changes estimated above. Therefore, based on above analysis we can safely rule out the coherent acoustic phonons.

G. π-phase difference between 820 nm and 800/780 nm for the ω_1 mode

We note there exists a π phase difference for the ω_1 mode using light with wavelengths between 820 nm and 780/800 nm. In fact, under the CDW phase, the state of investigated system can be described by an order parameter $\Psi = \Delta e^{i\phi}$, where the amplitude Δ and phase ϕ are functions of space and time. During discussion of the optical response, the dielectric constant within such phase transition can be expanded in powers of the order parameter [18]: $\epsilon \simeq \epsilon_0 + \alpha|\Psi|^2 = \epsilon_0 + \alpha\Delta^2$, where α is a constant solely determined by the intrinsic material properties. Therefore, fluctuation of the amplitude, $\delta\Delta$, can be given by: $\delta\epsilon \simeq 2\alpha\Delta_0\delta\Delta$, where Δ_0 is an equilibrium value, ϵ and α are complex numbers given by $\epsilon = \epsilon_r + i\epsilon_i$ and $\alpha = \alpha_r + i\alpha_i$, respectively.

On the other hand, in our experiment $\delta\Delta$ is directly manifested by the corresponding oscillatory transient reflectivity change $[\delta R]_{osc}$, i.e. $\delta\Delta \propto [\delta R]_{osc}$. Because $[\delta R]_{osc}$ can be related to ϵ by $[\delta R]_{osc} = \frac{\partial [R]_{osc}}{\partial \epsilon_r}\delta\epsilon_r + \frac{\partial [R]_{osc}}{\partial \epsilon_i}\delta\epsilon_i$ (Supplemental Material of Ref. [19]), we can obtain

$$[\delta R]_{osc} \propto \frac{\alpha_r}{2|\alpha|^2\Delta_0}\delta\epsilon_r + \frac{\alpha_i}{2|\alpha|^2\Delta_0}\delta\epsilon_i. \tag{7}$$

When we discuss the wavelength (λ) dependent behavior, since ϵ is a function of λ, we can rewrite the above equation as

$$[\delta R]_{osc} \propto \frac{1}{2|\alpha|^2\Delta_0}\left(\alpha_r\frac{\partial\epsilon_r}{\partial\lambda} + \alpha_i\frac{\partial\epsilon_i}{\partial\lambda}\right)\delta\lambda. \tag{8}$$

Based on such relation, if the coefficient, $\alpha_r\partial\epsilon_r/\partial\lambda + \alpha_i\partial\epsilon_i/\partial\lambda$, experiences a sudden sign reversal, then $\delta\Delta$ and its associated oscillatory signal $[\delta R]_{osc}$ should have an immediate π phase change.

Here, two points are needed to be clarified. (1) When we check the wavelength-dependent dielectric constants of ZrTe$_5$ [17], values of $\partial\epsilon_r/\partial\lambda$ (or $\partial\epsilon_i/\partial\lambda$) along a- and c-axis follow similar λ-dependence, and can undergo abrupt changes including the sign reversal around some anomalies near 820 nm ($\sim$1.5 eV). (2) Our experiments were carried out at low temperatures. Since with decreasing temperature the band gaps usually experience a blue shift ($dE_g/dT < 0$) causing a similar effect in absorption features of $\epsilon(\lambda)$, the related anomalies in $\epsilon_r(\lambda)$ and $\epsilon_i(\lambda)$ will experience a blue shift as well. Therefore, it is possible for these anomalies to reside between 780 nm ($\sim$1.59 eV) and 820 nm ($\sim$1.51 eV) at low temperatures.

Consequently, the coefficient, $\alpha_r\partial\epsilon_r/\partial\lambda + \alpha_i\partial\epsilon_i/\partial\lambda$, can undergo a sudden sign reversal and induce a π-phase difference in $\delta\Delta$ as the λ varies within the spectral regime of our experiment. Specifically, if the quasi-one dimensional ω_1 CDW mode (along b-axis) is a transverse mode with its amplitude determined by $(\partial\epsilon/\partial\lambda)_{a,c}$, its π-phase difference between 820 nm and 800/780 nm can then be reasonably explained in this way. We note that the magnitude of corresponding oscillation is also very sensitive to the above coefficient, as evidently revealed in Fig. 3(d) of the main text.

When discussing the phase change of high dimensional ω_2 CDW mode, we need to include contribution from the additional $(\partial\epsilon/\partial\lambda)_b$ term, which behaves quite differently from $(\partial\epsilon/\partial\lambda)_{a,c}$ in terms of their absolute values but also the signs, i.e. $(\partial\epsilon_r/\partial\lambda)_b > 0$ and $(\partial\epsilon_i/\partial\lambda)_b > 0$ for λ between $\sim$600 nm and $\sim$820 nm (or $h\nu$ between $\sim$1.5 eV and $\sim$2 eV). Therefore, if introducing the ϵ_b-related terms leads to the sign of above coefficient unchanged, the π-phase difference will not be observed as λ varies within the current spectral regime, as is confirmed by our experiments.

H. Oscillation signals including ω_1 and ω_2 modes as a function of pump fluence (F)
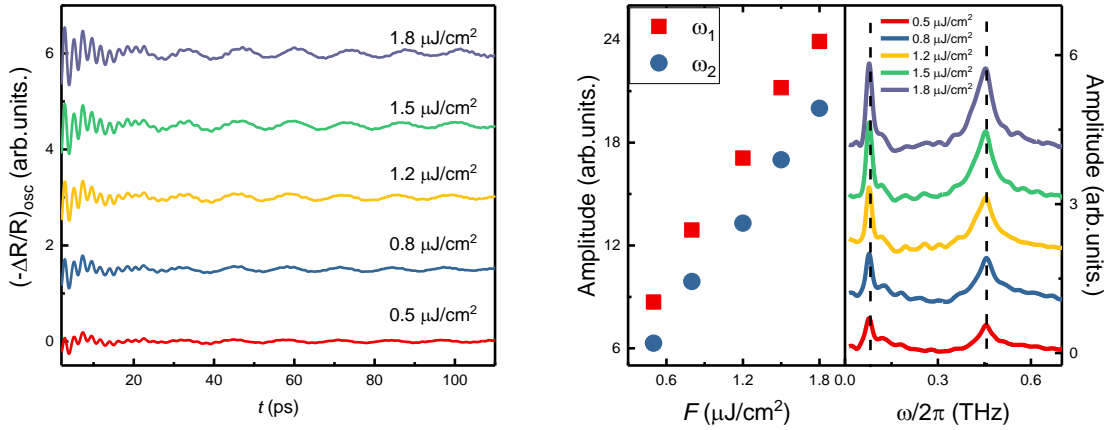

FIG. S6. (a) F-dependent oscillation signals $(\Delta R/R)_{osc}$ signals at 5 K for ω_1 and ω_2 modes. (b) F-dependent amplitudes and Fourier spectra from (a). Dashed lines indicate the peak positions of these two modes.

Fig. S6(a) shows the typical oscillation signals $(\Delta R/R)_{osc}$ as a function of F at 5 K extracted using a low pass frequency filter with a cutoff frequency of 1 THz. Overall, the signal strength increases with F. Our data fall within the linear regime, manifested clearly by the amplitude of the ω_1 and ω_2 modes linearly dependent on F, as shown in Fig. S6 (b). We also did not observe any frequency shift as the fluence changes.

I. Extraction of T-dependent fitting parameters for the ω_1 and ω_2 modes

Γ_j and $\omega_j/2\pi$ were obtained by fitting the experimental data using formula: $A_{\omega_j}e^{-\Gamma_j t}sin(\omega_j t + \phi_j)$ $(j = 1, 2)$. The oscillation data of ω_2 mode were first extracted using a 0.2-0.9 THz frequency filter to the original oscillatory signals. Typical fitting examples are shown in Fig. S7. The fitted amplitude A_{ω_1} and A_{ω_2} are also shown in Figs. S8(a) and (b). As shown in Fig. S8(c), in the decay process characterized by τ_s, no clear anomaly was observed near $T_C^{\omega_1}(\simeq 54$ K) in the temperature-dependent amplitude, $A_s(T)$, which, together with $\tau_s(T)$, further confirm that ω_1 mode can be ignored in discussing the potential bosons involved in the scattering process.
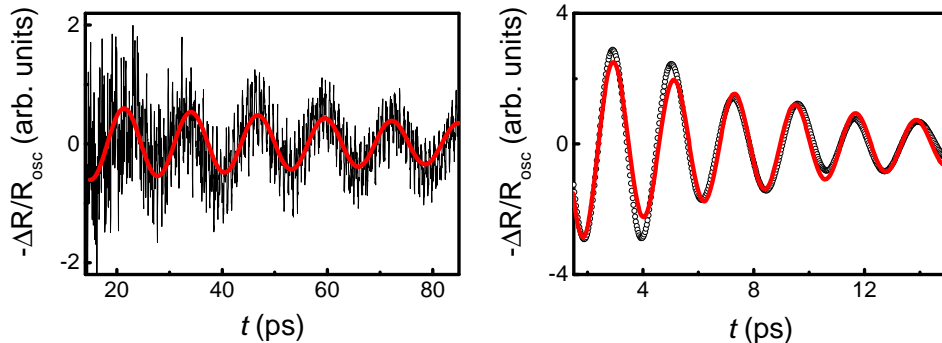

FIG. S7. (a) and (b) are typical oscillatory signals for ω_1 and ω_2 modes at 5 K, respectively. The red solid lines are examples for the fitting.
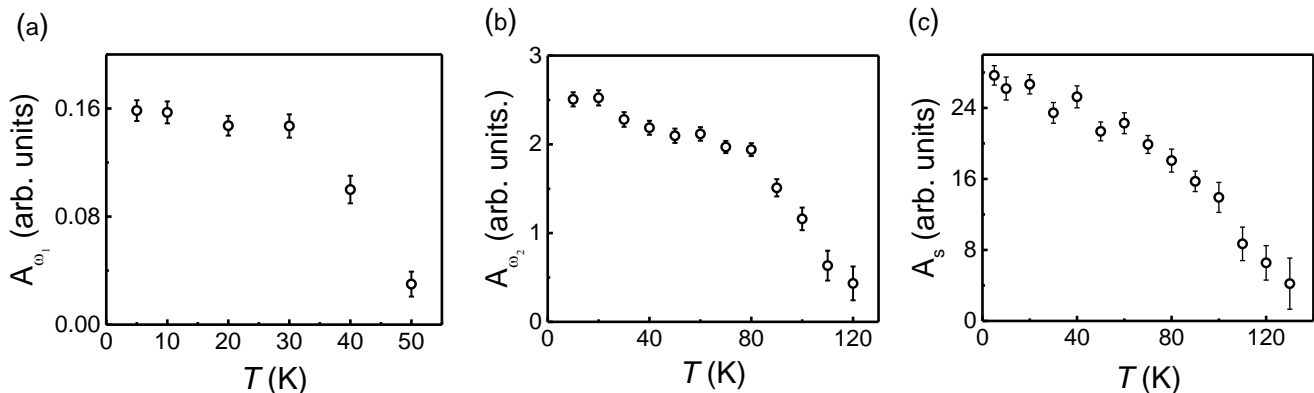

FIG. S8. (a) and (b) are fitted amplitudes for ω_1 and ω_2 modes as a function of temperature, respectively. (c) The fitted amplitude for τ_s relaxation process as a function of temperature.

J. Calculations of the phonon spectra and electron-phonon couplings in ZrTe$_5$

1. The Phonon spectra in STI and WTI phases

We calculated the phonon spectra of ZrTe$_5$ in the strong topological insulator (STI) phase and weak topological insulator (WTI) phase. The structure of WTI phase was obtained by the fully relaxed lattice which has larger interplane distance, whereas the structure of STI phase was taken from experiments [20, 21], which only have relaxation of the atom position but have no unit cell volume relexation. The phonon spectrum was calculated using the Quantum Espresso package [22, 23] via the density functional perturbation theory (DFPT) method [24]. In all the calculations, we used the GGA-PBE functional and norm-conserving potential [25]. We set the plane wave energy cutoff as 90 Ry and a $5 \times 5 \times 3k$-mesh. The spin-orbit coupling (SOC) was also considered in the calculations. The phonon spectra of both STI and WTI phases are shown in Fig. S9. In both cases, the lowest optical mode (with B_{1g} representation which has Raman activity) at Γ point is near 1 THz, which can be seen in Table II and III.
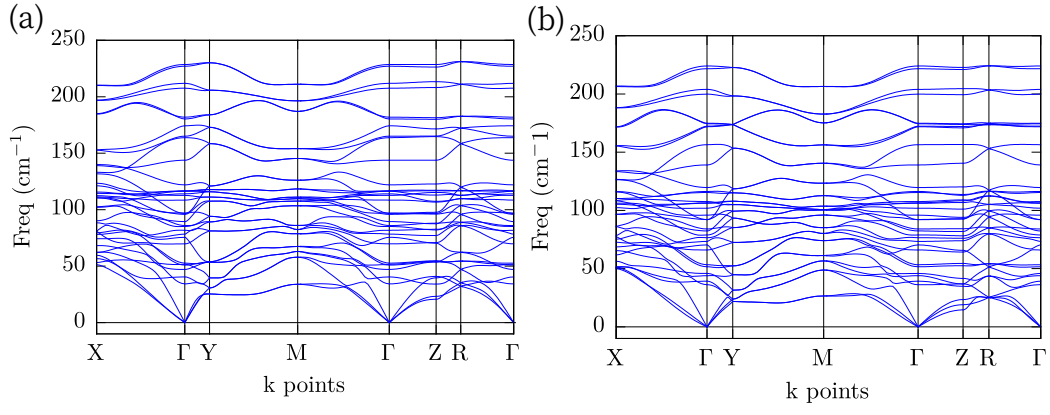
FIG. S9. The phonon spectra of (a) STI phase and (b) WTI phase. The lowest optical phonon mode (B_{1g} representation with Raman activity) at Γ point is near 1 THz.

TABLE II. The phonon frequency, representation, and active index (R or I) at Γ point for the STI phase. R and I represent the Raman and Infrared active modes, respectively. In our experiment, five Raman active modes were observed. According to Refs.[7, 8], three frequencies of $\sim$1.2 THz, $\sim$3.7 THz, $\sim$4.6 THz are attributed to the A_g phonon modes. The other two frequencies of $\sim$2.2 THz and $\sim$2.6 THz arise from the B_{2g} modes.

# mode	Frequency (THz)	Representation	Active Index
1	-0.0000	B_{3u}	I
2	-0.0000	B_{2u}	I
3	0.0000	B_{1u}	I
4	1.0275	B_{1g}	R
5	1.2118	B_{1u}	I
6	1.4118	A_g	R
7	1.5267	B_{2g}	R
8	1.5483	B_{2u}	I
9	1.5785	A_u	
10	2.0904	B_{1u}	I
11	2.2638	B_{3u}	I
12	2.3485	B_{2g}	R
13	2.4509	B_{3g}	R
14	2.5515	B_{1u}	I
15	2.5762	A_u	
16	2.6816	B_{2u}	I
17	2.8736	B_{1g}	R
18	2.8967	B_{3g}	R
19	2.9104	B_{2g}	R
20	3.2520	B_{3u}	I
21	3.3763	B_{1u}	I
22	3.4184	A_g	R
23	3.4864	B_{2g}	R
24	3.4914	A_g	R
25	3.4996	B_{3u}	I
26	3.6566	B_{1g}	R
27	4.3111	A_g	R
28	4.9099	B_{2g}	R
29	4.9485	A_g	R
30	5.2246	B_{3u}	I
31	5.4057	B_{1g}	R
32	5.4537	B_{2u}	I
33	6.2225	B_{2g}	R
34	6.3514	B_{1u}	I
35	6.8057	B_{3u}	I
36	6.8519	A_g	R

TABLE III. The phonon frequency, representation, and active index (R or I) at Γ point for the WTI phase. R and I represent the Raman and Infrared active modes, respectively. In our experiment, five Raman active modes were observed. According to Refs.[7, 8], three frequencies of $\sim$1.2 THz, $\sim$3.7 THz, $\sim$4.6 THz are attributed to the A_g phonon modes. The other two frequencies of $\sim$2.2 THz and $\sim$2.6 THz arise from the B_{2g} modes.

# mode	Frequency (THz)	Representation	Active Index
1	-0.0000	B_{3u}	I
2	-0.0000	B_{2u}	I
3	0.0000	B_{1u}	I
4	1.0842	B_{1g}	R
5	1.1749	B_{1u}	I
6	1.3171	A_g	R
7	1.3739	B_{2g}	R
8	1.5459	B_{2u}	I
9	1.5993	A_u	
10	1.9792	B_{1u}	I
11	2.1081	B_{3u}	I
12	2.1994	B_{2g}	R
13	2.2954	B_{3g}	R
14	2.3647	B_{1u}	I
15	2.4690	B_{2u}	I
16	2.5205	A_u	
17	2.7589	B_{3g}	R
18	2.7638	B_{1g}	R
19	2.8746	B_{2g}	R
20	3.0544	B_{3u}	I
21	3.1805	A_g	R
22	3.1929	B_{3u}	I
23	3.2260	B_{1u}	I
24	3.4584	B_{2g}	R
25	3.4855	A_g	R
26	3.5860	B_{1g}	R
27	4.1682	A_g	R
28	4.6901	B_{2g}	R
29	5.1528	A_g	R
30	5.1669	B_{1g}	R
31	5.2276	B_{2u}	I
32	5.2424	B_{3u}	I
33	5.9912	B_{2g}	R
34	6.1136	B_{1u}	I
35	6.6459	B_{3u}	I
36	6.7167	A_g	R

2. Calculations of the electron-phonon couplings

We also performed the calculation of the electron-phonon coupling to investigate the possible charge density wave (CDW) phase of ZrTe$_5$ using the EPW package [26, 27]. We choose the double-delta approximation to calculate the phonon linewidth. To get a converged result with increasing the density of k-mesh, we choose a $110 \times 110 \times 55$ fine k-mesh for STI phase and a $150 \times 150 \times 75$ k-mesh for WTI phase. Because the ordinary electronic state in DFT calculation is an insulator, we increased the Fermi level to get electron-type carriers with three kinds of carrier density as 4.97×10^{19} cm^{-3}, 2.27×10^{20} cm^{-3}, and 7.25×10^{20} cm^{-3}. The corresponding phonon linewidth of acoustic modes (the three lowest frequency phonon modes) are shown in Fig. S10. According to the phonon linewidth, we can
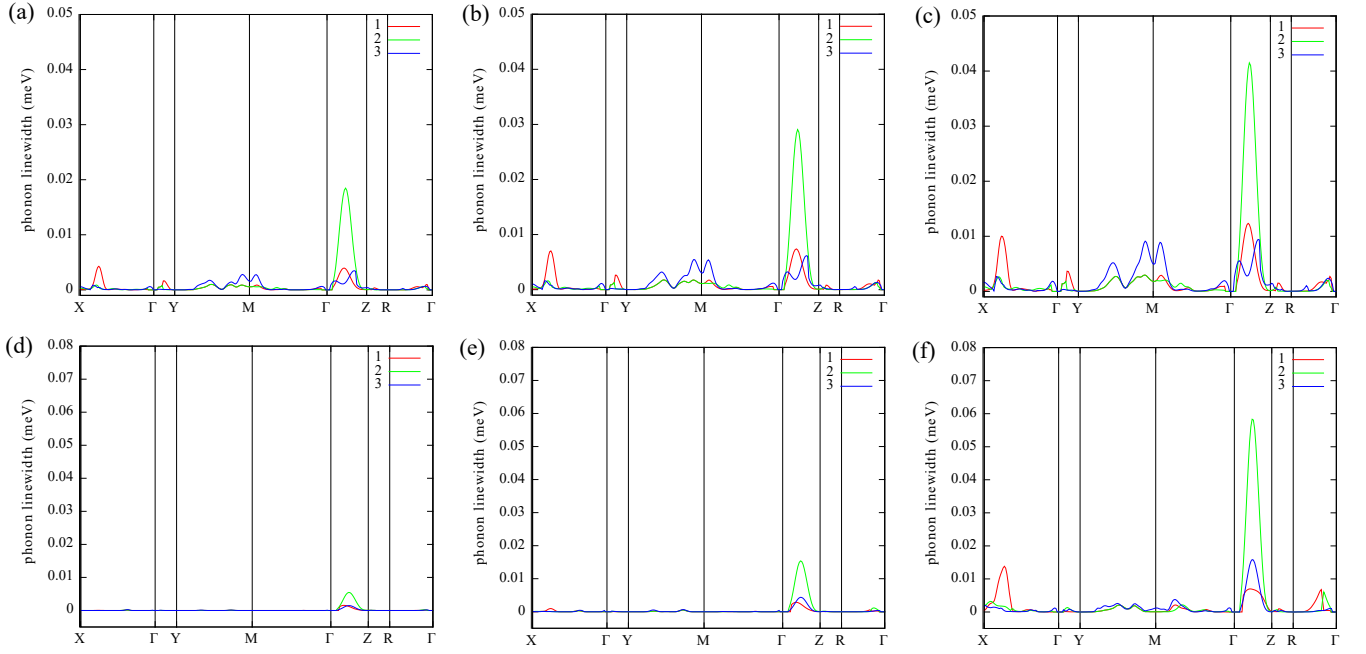
FIG. S10. The phonon linewidth of three acoustic modes (the three lowest frequency modes) corresponding to the carrier density of 4.97×10^{19} cm^{-3} [Fig. S10 (a) for STI phase, (d) for WTI phase], 2.27×10^{20} cm^{-3} [Fig. S10 (b) for STI phase, (e) for WTI phase] and 7.25×10^{20} cm^{-3} [Fig. S10 (c) for STI phase, (f) for WTI phase]. The convention of the high-symmetry points' label is the same as [28].

conclude that for both of the STI phase and WTI phase, the electron-phonon coupling in the inter-plane direction (Γ-Z direction) is stronger than those in the other directions. So the CDW phase can be mostly possible along the inter-plane direction (b-axis).

[1] T. Dekorsy, G. C. Cho, and H. Kurz, in Light Scattering in Solids VIII, Ed. by M. Cardona and G. Güntherodt (Springer, Berlin, 2000)

[2] Y. Jiang, Z. L. Dun, H. D. Zhou, Z. Lu, K.-W. Chen, S. Moon, T. Besara, T. M. Siegrist, R. E. Baumbach, D. Smirnov, and Z. Jiang, Phys. Rev. B **96**, 041101(R) (2017).

[3] Q. Li, D. E. Kharzeev, C. Zhang, Y. Huang, I. Pletikosic, A. V. Fedorov, R. D. Zhong, J. A. Schneeloch, G. D. Gu, and T. Valla, Nat. Phys. **12**, 550 (2016).

[4] P. B. Allen, Phys. Rev. B **6**, 2577 (1972).

[5] R. H. Groeneveld, R. Sprik, and A. Lagendijk, Phys. Rev. B **51**, 11433 (1995).

[6] A. A. Lopez, Phys. Rev. **175**, 823 (1968).

[7] A. Zwick, G. Landa, R. Carles, M. A. Renucci, and A. Kjekshus, Solid State Commun **44**, 89 (1982).

[8] Landa. G, Zwick. A, Carles. R, Renucci. M. A, Kjekshus. A. Solid state commun. **49**, 1095(1984).

[9] R. Merlin, Solid State Commun. **102**, 207 (1997).

[10] G. A. Garrett, T. F. Albrecht, J. F. Whitaker, and R. Merlin, Phys. Rev. Lett. **77**, 3661 (1996).

[11] I. Gdor, T. Ghosh, O. Lioubashevski, and S. Ruhman, J. Phys. Chem. Lett. **8**, 1920 (2017).

[12] G. Batignani, C. Ferrante, G. Fumero, and T. Scopigno, J. Phys. Chem. Lett. **10**, 7789 (2019).

[13] J. Qi et al., Phys. Rev. Lett. **111**, 057402 (2013).

[14] M. Balkanski, R. F. Wallis, and E. Haro, Phys. Rev. B **28**, 1928 (1983).

[15] J. Menendez and M. Cardona, Phys. Rev. B **29**, 2051 (1984).

[16] H. Tang and I. P. Herman, Phys. Rev. B **43**, 2299 (1991).

[17] Z. Guo, H. Gu, M. Fang, B. Song, W. Wang, X. Chen, C. Zhang, H. Jiang, L. Wang, and S. Liu, ACS Materials Lett. **3**, 525 (2021).

[18] V. L. Ginzburg, Sov. Phys. Usp. **5**, 649 (1963).

[19] Y. Toda, F. Kawanokami, T. Kurosawa, M. Oda, I. Madan, T. Mertelj, V. V. Kabanov, and D. Mihailovic, Phys. Rev. B **90**, 094513(2014).

[20] ZrTe$_5$ crystal structure: Datasheet from "pauling file multinaries edition – 2012" in springe materials (https://materials.springer.com/isp/crystallographic/docs/sd_0452870). Copyright 2016 Springer-Verlag Berlin Heidelberg &Material Phases Data System (MPDS), Switzerland & National Institute for Materials Science (NIMS), Japan.

[21] S. Furuseth, L. Brattas, and A. Kjekshus. J. Acta Chemica Scandinavica **27**, 2367 (1973).

[22] P. Giannozzi, S. Baroni, et al., J. Phys. Condens. Matter **21**, 395502 (2009).

[23] P. Giannozzi, O. Andreussi, et al., J. Phys. Condens. Matter **29**, 465901 (2017).

[24] S. Baroni, S. d. Gironcoli, A. D. Corso, and P. Giannozzi, Rev. Mod. Phys. **73**, 515 (2001).

[25] D. R. Hamann. Phys. Rev. B **88**, 085117 (2013).

[26] F. Giustino, M. L. Cohen, and S. G. Louie. Phys. Rev. B **76**, 165108 (2007).

[27] S. Poncé, E.R. Margine, C. Verdi, and F. Giustino. Comput Phys Commun **209**, 116 (2016).

[28] H. Weng, X. Dai, and Z. Fang, Phys. Rev. X **4**, 011002 (2014).